UV-assisted, template-free synthesis of ultrathin nanosheet-assembled hollow indium oxide microstructures for effective gaseous formaldehyde detection

Xue Wang [a,1], Yuying Meng [b,1], Guo-Dong Li [a], Yongcun Zou [a], Yang Cao [a], Xiaoxin Zou [a,*]

[a] State Key Laboratory of Inorganic Synthesis and Preparative Chemistry, International Joint Research Laboratory of Nano-Micro Architecture Chemistry, College of Chemistry, Jilin University, 2699 Qianjin Street, Changchun 130012, China
[b] School of Materials Science and Engineering, South China University of Technology, 381 Wushan Road, Tianhe District, Guangzhou 510640, China

ARTICLE INFO

ABSTRACT

Hollow micro-/nanostructures, especially those with well-defined nanoscale subunits, have been widely used in a variety of areas including catalysis, sensing, energy storage, drug delivery, etc. Herein, we report a novel, UV-assisted, template-free synthesis of hollow indium oxide microstructures that are composed of ultrathin nanosheets (~2.5 nm). The two key steps for the synthesis of the materials being successful are: (i) the UV-induced conversion of a photoactive solid indium alkoxide precursor into hollow indium hydroxide microspheres composed of ultrathin nanosheets, and (ii) the thermal treatment of the resulting hollow hydroxide microspheres into the hollow In_2O_3 material with a morphological preservation. Moreover, we show that the as-obtained hollow nanomaterials exhibit excellent sensing performance (e.g., high response value, good stability, as well as fast response speed) for the detection of ppm-level gaseous formaldehyde. The efficient sensing performance of the material is attributed to their overall conducive structural features, including their hollow architecture and ultrathin nanoscale building blocks. These structural features can offer a large amount of active sites on the surface, facilitate the diffusion and adsorption of the target gas, and thus enhance the material's sensing performance.

© 2015 Elsevier B.V. All rights reserved.

1. Introduction

Owing to their unique properties including low density, high specific surface area and remarkable permeability, hollow micro-/nanomaterials with various compositions have attracted great attention, and they have been widely used in a variety of areas including catalysis, sensing, energy storage, drug delivery, etc. [1–12]. Up to now, many efforts have been devoted to exploring the methods for the preparation of micro-/nanomaterials with designed hollow structures. One of the popular synthetic strategies is template-assisted one. The commonly used templates involve hard ones (e.g., silica, polymer, and carbon particles) [13,6,14], and soft ones (e.g., vesicles and emulsion droplets/micelles) [15–17]. However, templating methods for constructing hollow structures usually have some disadvantages such as high cost, multi-step tedious synthesis, long reaction time and strict reaction conditions. In contrast to the templating method, template-free synthesis

might be a more attractive strategy. With the rapid development of the template-free synthesis, some mechanisms, such as Kirkendall effect and Ostwald ripening, have recently appeared to explain such synthesis [18–20]. These positive results prompted us to explore further new template-free synthetic routes for the preparation of hollow structures with unique composition and nanoscale subunits as well as improved properties.

On the other hand, two-dimensional (2D) ultrathin nanomaterials with a thickness of <5 nm, such as graphene, have garnered increasing interest because the ultrathin nanostructures may lead to the increase in the number of surface active sites, as well as the exposure of some preferable crystallographic facets [21–23]. However, in contrast to the ease of making layered compounds into ultrathin 2D nanomaterials, it still maintains challenging to prepare such nanomaterials based on non-layered compounds, such as cubic Co_3O_4 [24–26]. This is mainly because these non-layered compounds generally have no spontaneous driving force for 2D anisotropic growth. Moreover, owing to their high surface energy, the ultrathin 2D nanomaterials have a very strong tendency to stack with each other during the material synthesis or application process. To resolve this problem, a feasible method is to assemble the ultrathin nanosheets into a three dimensional (3D)

* Corresponding author.
  E-mail addresses: xxzou@jlu.edu.cn, chemistryzouxx@gmail.com (X. Zou).
  [1] These authors contributed equally to this work.

structure. This will effectively avoid the nanosheets stacking, and thus retain the structural advantages of ultrathin morphology.

Herein, we report the synthesis of hollow In_2O_3 microspheres composed of ultrathin (~2.5 nm) nanosheets, for the first time. The synthesis of this material is achieved via a two-step method: (i) the UV-induced conversion of a photoactive solid indium alkoxide precursor into hollow indium hydroxide microspheres composed of ultrathin nanosheets, and (ii) the thermal treatment of the resulting hollow hydroxide microspheres into the hollow In_2O_3 material with a morphological preservation. The resulting hollow material combines the advantages of hollow structure and ultra-thin nanosheets in a single material system, and thus exhibits excellent sensing properties, such as high response value and fast response speed, for low-concentration gaseous formaldehyde detection. Although hollow In_2O_3 materials were previously reported, their syntheses were always assisted by various templates [27–33]. Additionally, the nanoscale subunits in those hollow In_2O_3 materials were usually the nanoparticles, and ultrathin nanosheets as the subunits were never reported before. Furthermore, our hollow In_2O_3 nanomaterial's sensing performance is also found to be better than that of most of the semiconductor materials reported recently for formaldehyde detection (Table S1).

2. Experimental

2.1. Chemicals and reagents

Indium (III) nitrate hydrate and glycerol were obtained from Sinopharm Chemical Reagent Co. Ltd (Shanghai, China). Isopropanol, ethanol and formaldehyde aqueous solution (37 wt%) were purchased from Beijing Chemical Works (Beijing, China). All the chemicals were used as received without further purification and distilled water was used throughout all experiments.

2.2. Synthesis of solid indium alkoxide microspheres (s-In-Alk)

The solid indium alkoxide microspheres were synthesized according to our previous work [34]. In details, 0.30 g $In(NO_3)_3 \cdot 4.5H_2O$ was firstly dissolved in 30 mL isopropanol under vigorous magnetic stirring, followed by adding 10 g glycerol. Subsequently, this resulting transparent mixture was transferred into a 50 mL Teflon-Lined autoclave and then treated at 180 °C for 1 h in an oven. After naturally cooled to the room temperature, the white precipitate (i.e., s-In-Alk precursor) was washed three times with ethanol to remove the residual inorganic ions and organic species. Finally, the s-In-Alk was dried in an oven at 80 °C for 12 h in air.

2.3. Preparation of hollow In_2O_3 microspheres from the s-In-Alk precursor

1 g of the s-In-Alk sample was dispersed in 100 mL deionized water and then irradiated with UV light for 2 h at room temperature. The UV-light source was a 125 W high-pressure mercury lamp (see the emission spectrum of this light source in Fig. S1), and the irradiation intensity of the UV-light was about 8.0×10^3 μW/cm². After irradiation, a fluffy sample was generated, and then this sold sample was washed twice with ethanol and dried in an oven at 80 °C for 12 h. This resulting powdered sample was denoted as UV-In-OH.

In order to obtain In_2O_3 materials, the In-OH was calcined at different temperatures (300, 400, 500, 600, or 700 °C) for 2 h in a muffle furnace in air with a heating rate of 2 °C/min. The as-prepared material was labelled as UV-In_2O_3-T, where T was the calcination temperature. For comparison, an In_2O_3 material (dubbed p-In_2O_3-400) was prepared by directly thermal treatment of s-In-Alk at 400 °C in air for 2 h.

2.4. Instrumentations and characterizations

The powder X-ray diffraction (XRD) patterns were performed with a Rigaku D/Max 2550 X-ray diffractometer using CuKα radiation (λ = 1.5418 Å) operated at 200 mA and 50 kV. The particle size and morphology were determined by transmission electron microscope (TEM, Philips-FEI Tecnai G2S-Twin), equipped with a field emission gun operating at 200 kV, and scanning electron microscope (SEM, JEOL JSM 6700F). The nitrogen adsorption and desorption isotherms were measured by a Micromeritics ASAP 2020M system. The infrared spectra (IR) were acquired with a Bruker IFS 66V/S FTIR spectrometer by placing the samples on pre-dried KBr pellets, from 4000 to 400 cm⁻¹ wavenumbers. UV–vis absorption spectra were recorded on a Perkin-Elmer Lambda 20 UV/vis spectrometer.

2.5. Sensor fabrication and testing

The In_2O_3 material was firstly mixed with a small amount of ethanol to make viscous slurry, followed by smoothly pasted using a small brush onto a designed ceramic tube (1 mm in diameter and 4 mm in length), which was attached with a pair of Au electrodes and four Pt wires on both ends of the tube. A Ni–Cr alloy coil passing through the ceramic tube was employed as a heater to adjust the operation temperature by tuning the heating current, and the operating temperature was measured on the surface of the sensor. The fabricated gas sensor was then aged at 200 °C for 12 h in air to enhance the stability and repeatability. The gas sensor was welded on a socket and gas sensing measurements were recorded on a commercial CGS-8 Gas Sensing Measurement System (Beijing Elite Tech Company Limited) using environmental air with a relative humidity of ~30% as both reference and diluting gas. Gas sensing properties were evaluated using a static test system which included a 1 L test chamber. In order to prepare the sample gases, a certain amount of formaldehyde aqueous solution (37 wt%) was transferred into the test chamber using a microsyringe and maintained for >120 min to give a homogenous atmosphere. To check the effect of water vapor on the formaldehyde response properties, pure water, in lieu of formaldehyde aqueous solution, was used in the preparation of sample gases. For measurement, the sensor was put into the test chamber to get a stable reading of resistance R_g. When the response reached a constant value, the sensor was taken out to recover in fresh air to get a stable reading of resistance of R_a. The sensor was tested at the temperature range of 80–260 °C and the formaldehyde concentration was in the variation of 1–100 ppm. The working principle of the sensor is shown in Scheme S1 in ESI. A load resistance (R_L) is connected in series to the sensor. The resistance of a sensor in air or a target gas was measured by the output signal voltage (V_{out}), i.e., the voltage at both ends of the load resistance, at a test circuit voltage of 5 V (V_s). The sensor response was defined as $S = R_a/R_g$, where R_a and R_g were the sensor resistance in environmental air and target gas, respectively.

3. Results and discussion

3.1. UV-induced synthesis of hollow indium hydroxide microspheres from the solid indium alkoxide precursor

The solid indium alkoxide microspheres were synthesized according to our previous work (for detailed characterization results of the precursor material, please see our previous report) [34]. This indium alkoxide precursor is denoted as s-In-Alk. SEM and
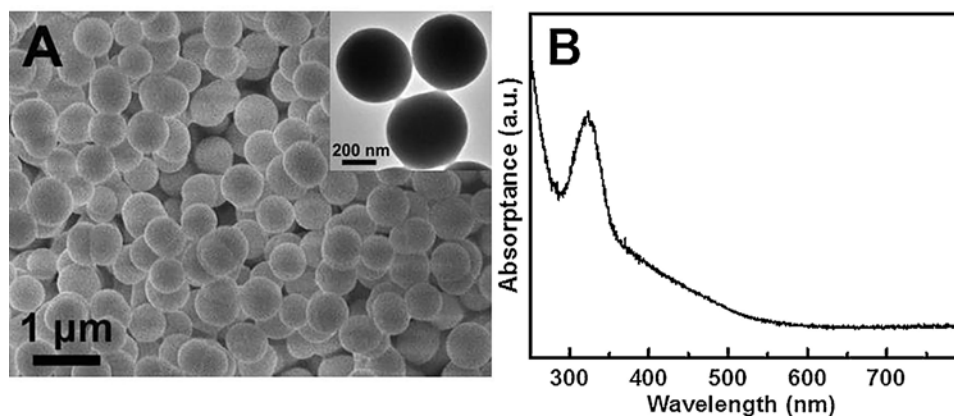
Fig. 1. (A) SEM image of s-In-Alk with its TEM image as the inset, and (B) UV–vis adsorption spectrum of s-In-Alk.

TEM images (Fig. 1A) show that the s-In-Alk precursor possesses a uniform solid sphere-like morphology with an average diameter of ∼450 nm. UV–vis adsorption spectrum shows that the s-In-Alk precursor is photoactive towards UV light, with an adsorption peak around 325 nm (Fig. 1B). This light response might be originated from the photo-excited electron transfer in InO$_x$ clusters that are embedded within the s-In-Alk precursor. Similar phenomena were also observed for titanium alkoxides in our previous reports [35–38].

Recently, we demonstrated that under light irradiation, some photoactive inorganic–organic hybrid compounds were transformed into novel inorganic functional materials that cannot be readily acquired using other approaches [35–39]. For example, we prepared ultrahigh surface area, nanoporous TiO$_2$ materials via UV-irradiation on the titanium alkoxides [35–38], and we also prepared ultrathin, porous ZnO nanosheets through UV-irradiation on a ZnS/cyclohexylamine hybrid precursor and subsequent calcination [39]. This light-driven route represents a novel synthetic method that is different from the traditional, widely used heat-driven synthetic route. These positive results, coupled with the photoactive feature of s-In-Alk, prompted us to elucidate the effect of light irradiation on the structural transformation of s-In-Alk.

Next, we treated the s-In-Alk in water with UV irradiation for 2 h at room temperature (see Section 2 for details). The resulting powered product was labelled as UV-In-OH. Fig. 2 shows the XRD patterns of UV-In-OH and s-In-Alk. From Fig. 2, it is clearly seen
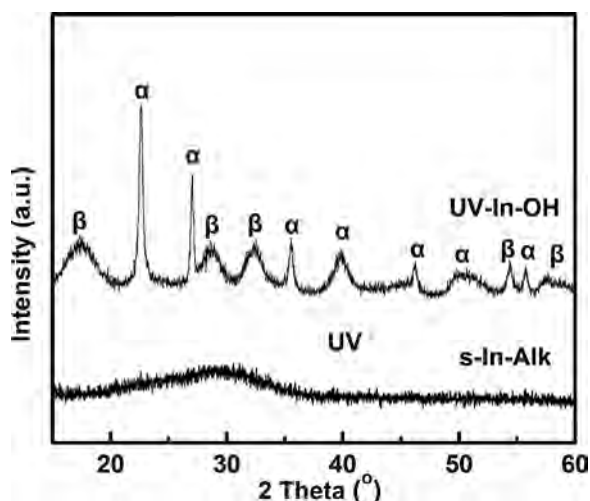
that s-In-Alk is an amorphous material, and after irradiation it is transformed into a crystalline UV-In-OH product. The XRD pattern of UV-In-OH is indexed as a mixture of two crystalline phases: cubic phase In(OH)$_3$ (i.e., α-In(OH)$_3$) and orthorhombic phase InOOH (i.e., β-InOOH). The co-existence of α-In(OH)$_3$ and β-InOOH is not unusual because α-In(OH)$_3$ is readily transformed into β-InOOH by losing one molar water molecule [40]. Additionally, the comparison of IR absorption spectra (Fig. S2) of UV-In-OH and s-In-Alk reveals that the IR absorption bands related to the organic component completely disappear after 2 h UV irradiation. The XRD and IR results indicate that after exposed to UV irradiation, the s-In-Alk loses its organic components and is converted to the UV-In-OH with a crystalline structure. It is worth noting that UV irradiation is necessary for the transformation from s-In-Alk to UV-In-OH. This is because when no UV irradiation was used, under otherwise identical reaction conditions as the one we employed above, the structure of s-In-Alk retained intact. Similar to our previous reports [35–39], the inherent driving force for the transformation from s-In-Alk to UV-In-OH should be the generation of photoexcited charges in the inorganic component of s-In-Alk. The photogenerated charges can initiate a series of redox reactions to remove the organic component in the s-In-Alk, and meanwhile, inorganic species can react with water to form a new compound (i.e., UV-In-OH).

The morphological and microstructural analyses of UV-In-OH were carried out using SEM and TEM (Fig. 3). SEM image (Fig. 3A) shows that UV-In-OH has a sphere-like morphology, and these microspheres are uniform in shape and size with an average diameter of c.a. 800 nm. Some broken microspheres with clear interior cavities are observed in Fig. 3A, indicating that the UV-In-OH microspheres have a hollow structure. In addition, Fig. 3B shows the UV-In-OH microsphere is composed of numerous two-dimensional ultra-thin nanosheets, which self-assemble perpendicularly on the spherical surface. This unique 3D nanosheet-assembled hollow microstructure of UV-In-OH was further verified by TEM measurement. The TEM image of UV-In-OH (Fig. 3C) shows a lighter region at the centre and a continuous darker region around the edges of the UV-In-OH microspheres, confirming the presence of the nanosheet-assembled hollow structure. These nanosheets are very thin, with a typical thickness ranging from 2.0 to 2.7 nm (Fig. 3D).

In order to investigate the morphology evolvement from s-In-Alk to UV-In-OH under UV irradiation, time-dependent experiments were carried out by varying the UV irradiation time on the s-In-Alk precursor. TEM image (Fig. 4A) demonstrates that the s-In-Alk precursor contains solid microspheres with a smooth surface. When the s-In-Alk precursor was exposed to UV light for 60 min (Fig. 4B), a large amount of ultrathin nanosheets formed around the edges of the s-In-Alk microspheres. When the irradiation time was prolonged to 75 min (Fig. 4C), the volume of the solid s-In-Alk
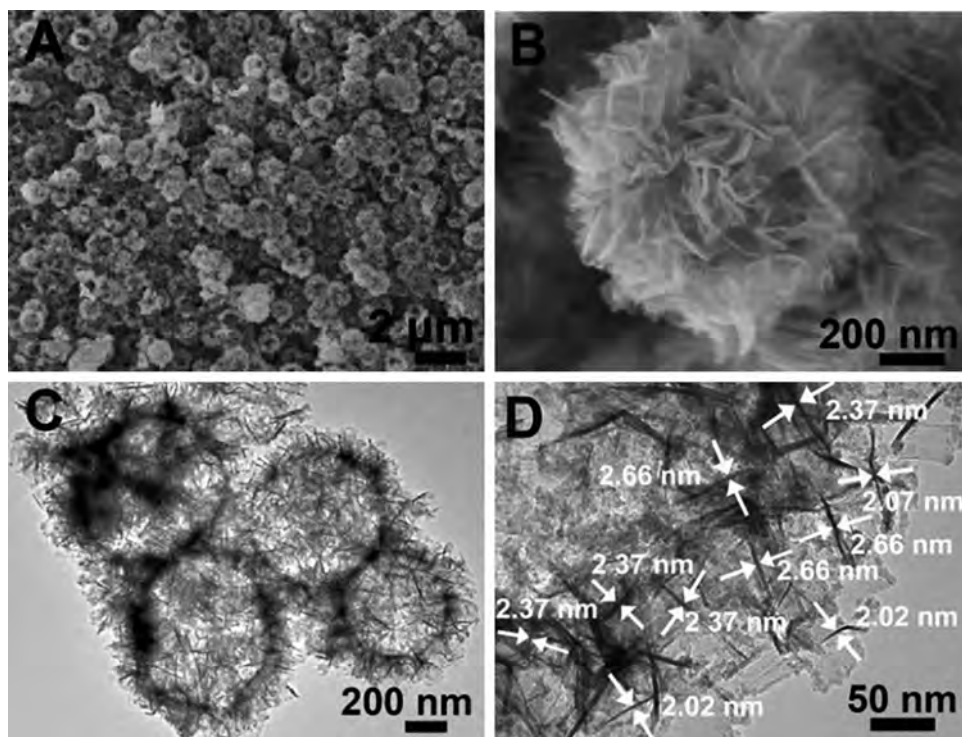

Fig. 2. XRD patterns of UV-In-OH and s-In-Alk. α and β in the figure stand for α-In(OH)$_3$ and β-InOOH, respectively.

Fig. 3. (A, B) SEM images and (C, D) TEM images of UV-In-OH.

microsphere markedly reduced, and meanwhile, the amount of the nanosheets increased a lot, leading to the formation of a core–shell-type structure. Further extending the irradiation time to 120 min led to the final formation of flower-like hierarchical microspheres with a hollow structure (Fig. 4D). This morphology evolvement can be explained by UV-light driven formation of ultrathin nanosheet-assembled indium hydroxide hollow structure from the solid s-In-Alk precursor. In details, the UV-In-OH nanosheets were firstly generated on the microsphere surfaces with the scarcity of exterior s-In-Alk, followed by the gradual consumption of the inner s-In-Alk and the formation of UV-In-OH nanosheets with the increase in UV irradiation time. And finally, the s-In-Alk was completely consumed and UV-In-OH nanosheets were well assembled into a 3D hierarchical spherical hollow structure (Fig. 4D).

On the basis of the above experimental observations, we suggested that the formation of flower-like hierarchical hollow UV-In-OH microsphere likely followed the Kirkendall effect driven by the hydrolysis reaction between s-In-Alk and water (Scheme 1) [18,19]. As shown in Scheme 1, the surface of s-In-Alk should first react with water to yield a thin layer of indium hydroxide. Once the s-In-Alk surface was fully covered by the indium hydroxide microcrystals, the further conversion of inner s-In-Alk would have

to occur via the outward diffusion of indium species across the interface. The constant consumption of s-In-Alk leads to the formation of voids at the s-In-Alk/UV-In-OH interface. Eventually, the entire s-In-Alk core was completely consumed, resulting in the production of a hollow UV-In-OH microsphere. Because both α-In(OH)$_3$ and β-InOOH have a layered crystal structure, they will exhibit a very strong tendency to form sheet-like nanocrystals. This is also why nanosheet morphology finally dominates the whole UV-In-OH microstructures.

3.2. Formation of hollow In$_2$O$_3$ microspheres from UV-In-OH

The UV-In-OH can be easily thermally transformed into In$_2$O$_3$ materials in air. The as-prepared material was labelled as UV-In$_2$O$_3$-T, where T was the calcination temperature. Note that In$_2$O$_3$ materials form only at or above 300 °C. Fig. 5 shows the XRD patterns of a series of In$_2$O$_3$ materials obtained by the thermal treatment of UV-In-OH at different temperatures (300, 400, 500, 600, or 700 °C) in air. As shown in Fig. 5, all the samples exhibit similar XRD patterns that are indexed as cubic In$_2$O$_3$. In addition, the increase in the calcination temperature lead to the obvious increase in the intensities of XRD peaks, probably originated from the improved crystallinity of cubic In$_2$O$_3$. Furthermore,
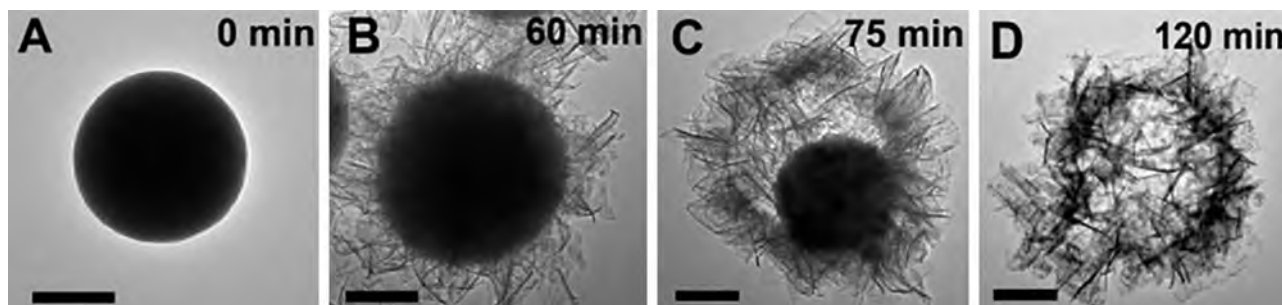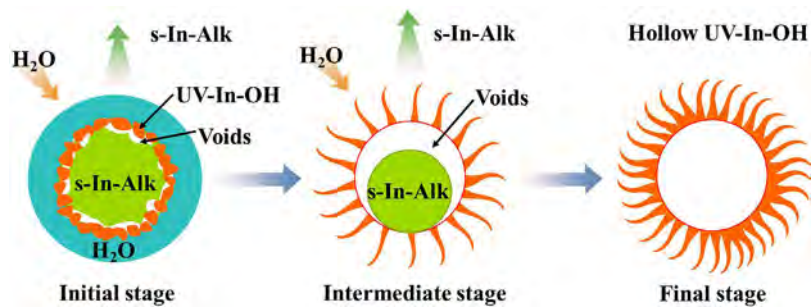

Fig. 4. TEM images of the products obtained after UV-irradiation on s-In-Alk for (A) 0 min, (B) 60 min, (C) 75 min and (D) 120 min. Scale bars: 200 nm.

Scheme 1. Schematic illustration for the formation of hollow UV-In-OH microsphere from s-In-Alk via Kirkendall effect.
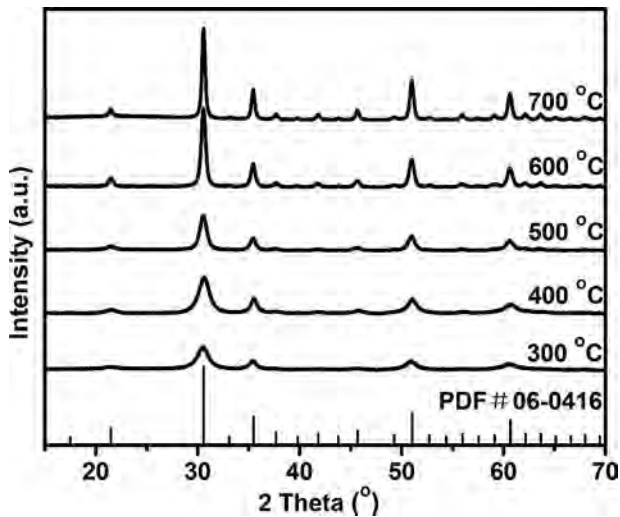

Fig. 5. XRD patterns of a series of In_2O_3 materials obtained by the thermal treatment of UV-In-OH at different temperatures in air. The standard XRD card of the Joint Committee on Powder Diffraction Standards (JCPDS) for In_2O_3's (PDF#06-0416) is also shown in this figure, for comparison.

no impurity phases are detected apart from the cubic In_2O_3 in all samples, indicating that pure In_2O_3 phase has been successfully obtained from UV-In-OH by a facile thermal treatment. Because UV-In_2O_3-400 shows the best sensing performance among all the samples, some of the characterizations below are focused on this material.

The morphology and crystal phase of UV-In_2O_3-400 were further investigated by SEM and TEM. Fig. 6A and B shows the SEM images of UV-In_2O_3-400. The SEM images reveal that UV-In_2O_3-400 maintains the morphology, size and sheet-like nanosized building blocks of UV-In-OH. These UV-In_2O_3-400 microspheres with a diameter of about 800 nm are relatively uniform, and they are composed of well-defined nanosheets with a thickness of ~2.5 nm, as revealed by the TEM image (Fig. 6C). In the HRTEM image (Fig. 6D), the observed lattice spacing is about 0.29 nm, which corresponds to the distance between the (222) crystal planes of the cubic In_2O_3 phase. Additional SEM results on other UV-In_2O_3-T samples (Fig. S3) reveal that besides UV-In_2O_3-400, UV-In_2O_3-300 can also maintain the morphology of UV-In-OH, but the nanosheet-assembled hollow structure for the samples obtained at or above 500 °C are destroyed to a great extent.
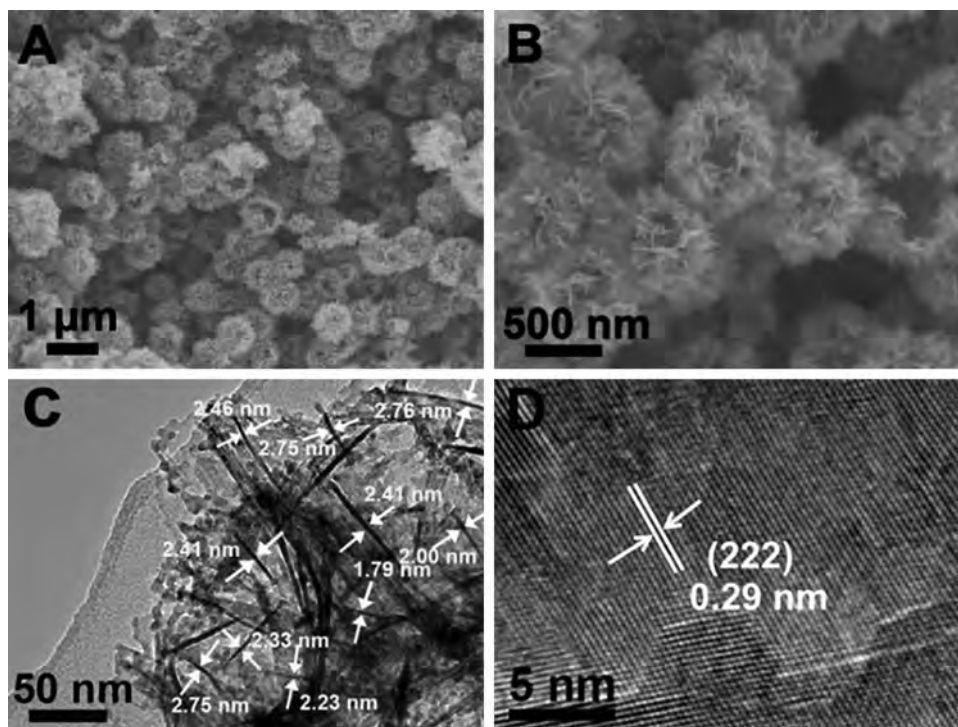

Fig. 6. (A, B) SEM images, (C) TEM and (D) HRTEM images of UV-In_2O_3-400.
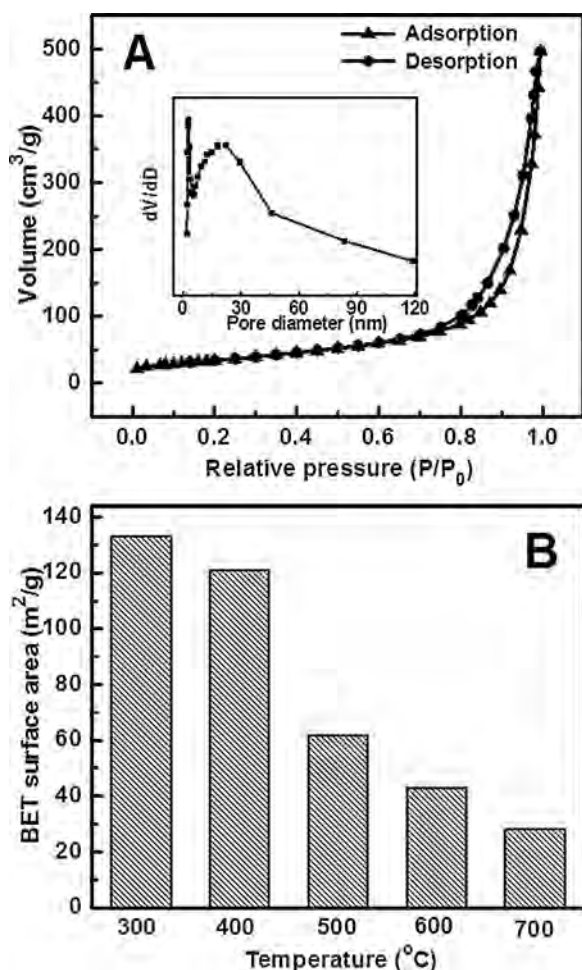
Fig. 7. (A) Nitrogen gas adsorption/desorption isotherms of UV-In$_2$O$_3$-400, with the corresponding pore size distribution shown in the inset. (B) The comparison of the BET surface area of the UV-In$_2$O$_3$-T sample obtained at different temperatures.

Fig. 7A demonstrates the nitrogen gas adsorption/desorption isotherms and BJH pore size distribution curve of UV-In$_2$O$_3$-400. The N$_2$ adsorption/desorption isotherms of UV-In$_2$O$_3$-400 are of typical type-IV with an H1-type hysteresis loop, indicating the presence of a mesoporous/macroporous structure in the material. The corresponding BJH pore size distribution analysis was inserted in Fig. 7A, and the result shows that the material has a wide pore size distribution was ranging from 2 to 120 nm. The broad pore-size distribution should be associated with the interspaces formed by the adjacent nanosheets. In addition, the BET surface area of the material is found to be 121 m^2/g. We also compared the BET surface area of the samples obtained at different temperatures (Fig. 7B). The result reveals that the BET surface area gradually decreased with the increase in the treatment temperature, ranging from 133 to 28 m^2/g for UV-In$_2$O$_3$-300 and UV-In$_2$O$_3$-700, respectively.

For a comparative purpose, one more sample (dubbed p-In$_2$O$_3$-400) was prepared by direct thermal treatment of the s-In-Alk precursor at 400 °C in air. Detailed characterization on this material can be found in our previous report [34]. Different from UV-In$_2$O$_3$-400, the p-In$_2$O$_3$-400 material contains nanoparticle-assembled microspheres (SEM images in Fig. S4), and has a BET surface area of 38 m^2/g. It is obvious that the BET surface area of UV-In$_2$O$_3$-400 is much larger than that of p-In$_2$O$_3$-400, and the former is >3 times as high as that of the latter.

3.3. Sensing performance of ultrathin nanosheet-assembled hollow indium oxide

In$_2$O$_3$ is an important sensing material that changes its electrical resistance in response to changes in the nearby chemical environment. In view of the structural advantages of ultrathin nanosheet-assembled hollow In$_2$O$_3$ materials, we next investigated their sensing performance towards the detection of formaldehyde, a toxic and carcinogenic gas. Detailed procedures for the sensor fabrication can be found in Section 2. Because the operating temperature of a sensor is tightly related to its sensing properties, we first determined the optimal operating temperature of the sensor based on UV-In$_2$O$_3$-400 (Fig. 8). In order to achieve this goal, we took into consideration three important factors: the response value, the response time and the recovery time. The sensor response is defined as the ratio R_a/R_g, where R_a and R_g are the electrical resistances of the sensor in atmospheric air and in the formaldehyde gas, respectively. The response and recovery times are defined as the times taken by the sensor to achieve 90% of the total resistance change in the target gas and in the fresh air, respectively. As shown in Fig. 8A, the UV-In$_2$O$_3$-400 sensor shows good response to the formaldehyde gas throughout the operating temperature range (80–260 °C), with the highest response as high as 1440 at 110 °C. In addition, the response time for the UV-In$_2$O$_3$-400 sensor is very fast (<12 s) throughout the operating temperature range (Fig. 8B). Especially, when the operating temperature is >140 °C, the response time for the UV-In$_2$O$_3$-400 sensor is even lower than 5 s. Furthermore, in Fig. 8C, it is seen that when the operating temperature was <200 °C, the resistance of the sensor is unable to be recovered. Hence, based on the factors mentioned above, 200 °C was selected as the optimized operating temperature, due to its relatively high response value ($R_a/R_g = 43$), fast response time (<2 s) and acceptable recovery time (~483 s). All further sensing measurements were conducted at this optimal operating temperature.

The representative response–recovery curve of UV-In$_2$O$_3$-400 sensor with increasing formaldehyde concentrations (1–100 ppm) is displayed in Fig. 9A. This figure reveals that the sensor has a wide response range for formaldehyde gas from 1 to 100 ppm. Upon exposing in 1 ppm formaldehyde, the resistance of the sensor rapidly decreases from ~400 kΩ (in air) to ~295 kΩ, and when the sensor is exposed to air again, the resistance returns to the original value. Similar response and recovery behaviours are also observed for the detection of higher concentration formaldehyde gas. The main difference lies in a higher formaldehyde concentration giving a lower resistance value. For formaldehyde concentrations of 2, 5, 10, 20, 50, 75 and 100 ppm, the resistances are about 155, 50, 28, 18, 13, 11, 8 kΩ, respectively. To check the effect of water vapor on the formaldehyde response properties, pure water, in lieu of formaldehyde aqueous solution, was used in the preparation of sample gases. The sensing results show that water vapor almost have no effect on the detection of formaldehyde (Figs. 9A and S5). In addition to the concentration-dependent response, the UV-In$_2$O$_3$-400 sensor shows excellent signal stability. This is confirmed based on the response-recovery curve after 15 cycles in the presence of 10 ppm formaldehyde, which is almost the same as the original one (Fig. 9B). Furthermore, the UV-In$_2$O$_3$-400 sensor has a fast response behaviour, with the response times of 22, 6, 8, 2, 2, 2, 2, 2 s for variable formaldehyde concentrations of 1, 2, 5, 10, 20, 50, 75 and 100 ppm, respectively. The recovery time is less than 500 s throughout the concentration range from 1 to 100 ppm. The quick response and recovery properties might be due to the presence of the 3D flower-like hollow nanostructure that is very beneficial for the gas diffusion.

The resistance decrease of In$_2$O$_3$ upon exposure to the formaldehyde gas (or In$_2$O$_3$'s sensing behaviour) can be explained by the
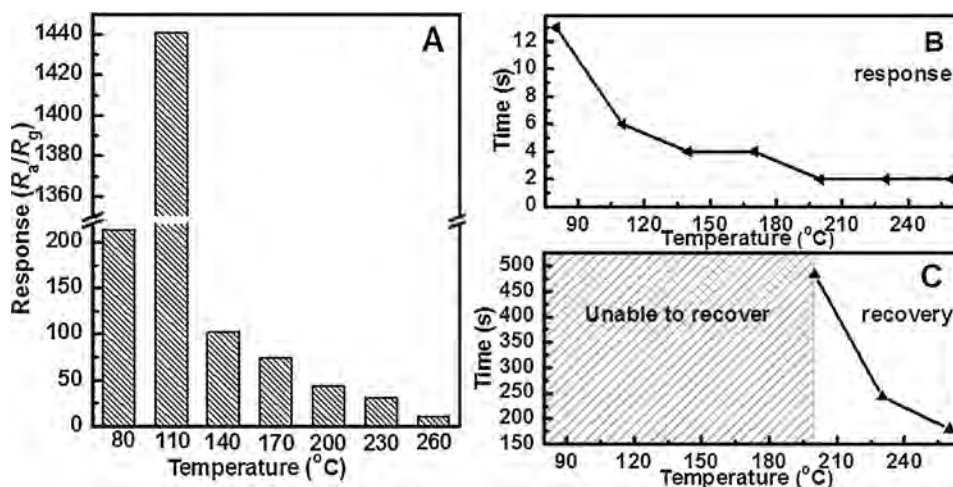
Fig. 8. Determination of the optimal operating temperature of the sensor based on UV-In$_2$O$_3$-400. (A) The response value, (B) the response time and (C) the recovery time of the sensor as a function of the operating temperature for the detection of formaldehyde with a concentration of 50 ppm.

chemical interaction of formaldehyde with In$_2$O$_3$, a typical n-type semiconductor (see Scheme S2) [34,41–56]. First, a certain amount of oxygen molecules in air are chemisorbed on the In$_2$O$_3$ surface, and they can extract electrons from the conduction band of In$_2$O$_3$, leading to the creation of a potential barrier and thus a high resistance state. When the In$_2$O$_3$ sensor is exposed to the formaldehyde gas at an elevated temperature (200 °C in this work), the reaction between formaldehyde and the surface oxygen species takes place, resulting in a decrease in the amount of adsorbed oxygen species. As a result, the height of the potential barrier is reduced, and the resistance of In$_2$O$_3$ decreases correspondingly. However, when the sensor is operated at low temperatures (e.g., less than 100 °C in our work), the direct electron transfer from organic molecules to the semiconductor In$_2$O$_3$ likely causes the resistance decrease because the oxidation of the organic molecules at low temperatures

is not easy and the resistance recovery (probably companied by the desorption of organic molecules) is not observed in this case. Further in-depth mechanistic investigation, especially for the complicated interplay between organic molecules and semiconductor oxides at different operating temperature, is underway, and we hope to report on it in due course.

In order to uncover the interplay between the structures and the sensing performance of the materials, we prepared a series of relevant samples by varying the temperature of thermal treatment on UV-In-OH (see above), and compared their sensing properties. As shown in Fig. 10, the sensor response increases when the calcination temperature increases from 300 to 400 °C, and it then decreases when the calcination temperature is further increased, from 500 to 700 °C, with the material obtained at 400 °C (i.e., UV-In$_2$O$_3$-400) possessing the best sensing performance. The observed difference of sensing performance should correlate with the inherent structural difference of the materials. With the increase in the thermal treatment temperature of UV-In-OH from 400 to 700 °C, the nanosheet-assembled hollow structure of the resulting In$_2$O$_3$ material was largely destroyed (Fig. S3), and the BET surface area of the material was also reduced a lot (Fig. 7B). Generally, the larger surface area of the sensing material results in higher density of
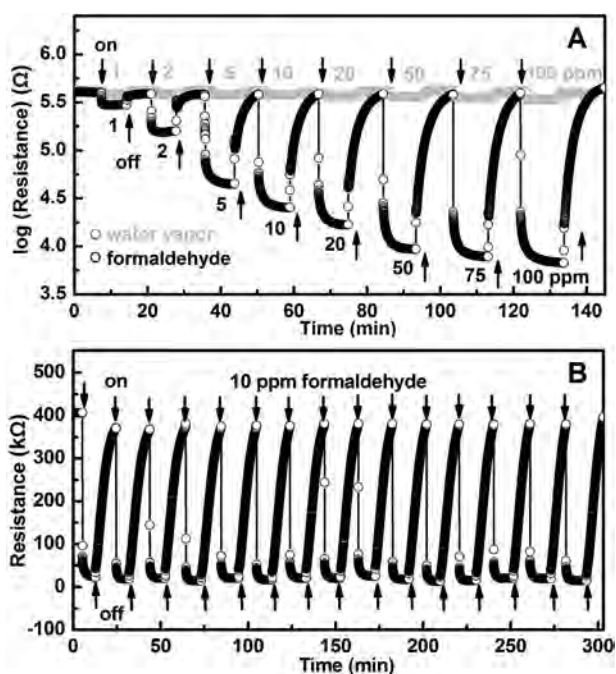

Fig. 9. (A) A response–recovery curve of the UV-In$_2$O$_3$-400 sensor with increasing formaldehyde concentrations (1–100 ppm) at an operating temperature of 200 °C. (B) A response–recovery curve of the UV-In$_2$O$_3$-400 sensor for continuous detection in the presence of 10 ppm formaldehyde at an operating temperature of 200 °C.

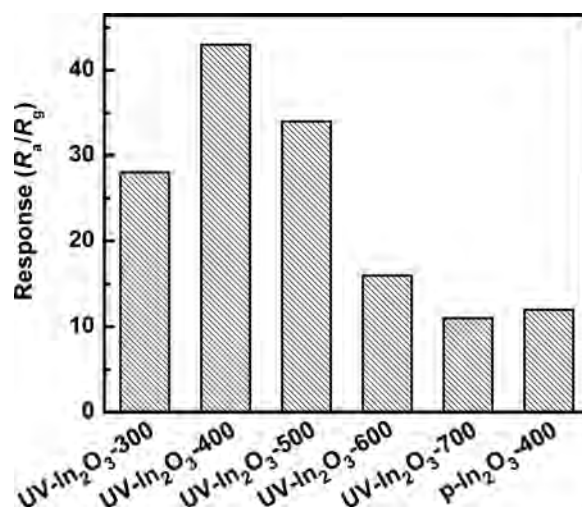**Fig. 10.** Comparison of the responses towards 50 ppm formaldehyde of several sensors based on UV-In$_2$O$_3$-300, UV-In$_2$O$_3$-400, UV-In$_2$O$_3$-500, UV-In$_2$O$_3$-600, UV-In$_2$O$_3$-700, or p-In$_2$O$_3$-400 at an operating temperature of 200 °C.

surface reactive sites and greater contact area with the target gas, and thereby showing better sensing property. Taking into account the fact that UV-In_2O_3-300 and UV-In_2O_3-400 possess a similar morphology and the former has a little higher surface area and lower sensing response than the latter, it is indicative that besides the surface area, the crystallinity of the material might play an important role in determining the gas sensing performance of In_2O_3 because of UV-In_2O_3-400's higher crystallinity than UV-In_2O_3-300. Furthermore, it is worth noting that the UV-In_2O_3-400 material exhibits much better response towards formaldehyde than p-In_2O_3-400, which is prepared by direct thermal treatment of the s-In-Alk precursor at 400 °C in air (see above). Overall, the excellent sensing performance of UV-In_2O_3-400 is attributed to the synergistic effect originated from its hollow architecture and its ultrathin nanoscale building blocks. These structural features can offer a large amount of active sites on the surface, facilitate the diffusion and adsorption of the target gas, and thus enhance the material's sensing performance.

4. Conclusions

In summary, we report a unique UV-assisted, template-free synthetic route to prepare hollow indium oxide microstructures that are composed of ultrathin nanosheets (∼2.5 nm). We also show that the resulting hollow nanomaterials exhibit excellent sensing performance (e.g., high response value, good stability, as well as fast response speed) for the detection of ppm-level gaseous formaldehyde. Our results could encourage further research on light-assisted methods for the synthesis of various inorganic nanomaterials with unique composition and morphology as well as enhanced properties.

Acknowledgments

Appendix A. Supplementary data

Supplementary data associated with this article can be found, in the online version, at http://dx.doi.org/10.1016/j.snb.2015.10.100.

References

[1] X.W. Lou, L.A. Archer, Z. Yang, Hollow micro-/nanostructures: synthesis and applications, Adv. Mater. 20 (2008) 3987–4019.
[2] C. Yuan, H.B. Wu, Y. Xie, X.W. Lou, Mixed transition-metal oxides: design, synthesis, and energy-related applications, Angew. Chem. Int. Ed. 53 (2014) 1488–1504.
[3] A. Pan, H.B. Wu, L. Yu, X.W. Lou, Template-free synthesis of VO_2 hollow microspheres with various interiors and their conversion into V_2O_5 for lithium-ion batteries, Angew. Chem. 125 (2013) 2282–2286.
[4] B. Wang, J.S. Chen, H.B. Wu, Z. Wang, X.W. Lou, Quasiemulsion-templated formation of α-Fe_2O_3 hollow spheres with enhanced lithium storage properties, J. Am. Chem. Soc. 133 (2011) 17146–17148.
[5] X.W. Lou, Y. Wang, C. Yuan, J.Y. Lee, L.A. Archer, Template-free synthesis of SnO_2 hollow nanostructures with high lithium storage capacity, Adv. Mater. 18 (2006) 2325–2329.
[6] X. Wang, X.-L. Wu, Y.-G. Guo, Y. Zhong, X. Cao, Y. Ma, J. Yao, Synthesis and lithium storage properties of Co_3O_4 nanosheet-assembled multishelled hollow spheres, Adv. Funct. Mater. 20 (2010) 1680–1686.
[7] J. Zhao, Y. Zou, X. Zou, T. Bai, Y. Liu, R. Gao, D. Wang, G.-D. Li, Self-template construction of hollow Co_3O_4 microspheres from porous ultrathin nanosheets and efficient noble metal-free water oxidation catalysts, Nanoscale 6 (2014) 7255–7262.
[8] J. Liu, S.Z. Qiao, S.B. Hartono, G.Q. Lu, Monodisperse yolk–shell nanoparticles with a hierarchical porous structure for delivery vehicles and nanoreactors, Angew. Chem. Int. Ed. 49 (2010) 4981–4985.
[9] Y. Zhu, J. Shi, W. Shen, X. Dong, J. Feng, M. Ruan, Y. Li, Stimuli-responsive controlled drug release from a hollow mesoporous silica sphere/polyelectrolyte multilayer core–shell structure, Angew. Chem. Int. Ed. 44 (2005) 5083–5087.
[10] X. Lai, J. Li, B.A. Korgel, Z. Dong, Z. Li, F. Su, J. Du, D. Wang, General synthesis and gas-sensing properties of multiple-shell metal oxide hollow microspheres, Angew. Chem. 123 (2011) 2790–2793.
[11] Y.-T. Wang, W.-T. Whang, C.-H. Chen, Hollow V_2O_5 nanoassemblies for high-performance room-temperature hydrogen sensors, ACS Appl. Mater. Interfaces 7 (2015) 8480–8487.
[12] H.-J. Kim, H.-M. Jeong, T.-H. Kim, J.-H. Chung, Y.C. Kang, J.-H. Lee, Enhanced ethanol sensing characteristics of In_2O_3-decorated NiO hollow nanostructures via modulation of hole accumulation layers, ACS Appl. Mater. Interfaces 6 (2014) 18197–18204.
[13] X.W. Lou, C. Yuan, L.A. Archer, Double-walled SnO_2 nano-cocoons with movable magnetic cores, Adv. Mater. 19 (2007) 3328–3332.
[14] Z. Dong, X. Lai, J.E. Halpert, N. Yang, L. Yi, J. Zhai, D. Wang, Z. Tang, L. Jiang, Accurate control of multishelled ZnO hollow microspheres for dye-sensitized solar cells with high efficiency, Adv. Mater. 24 (2012) 1046–1049.
[15] Y. Zhang, M. Yu, L. Zhou, X. Zhou, Q. Zhao, H. Li, C. Yu, Organosilica multilamellar vesicles with tunable number of layers and sponge-like walls via one surfactant templating, Chem. Mater. 20 (2008) 6238–6243.
[16] H. Xu, W. Wang, Template synthesis of multishelled Cu_2O hollow spheres with a single-crystalline shell wall, Angew. Chem. Int. Ed. 46 (2007) 1489–1492.
[17] D. Walsh, B. Lebeau, S. Mann, Morphosynthesis of calcium carbonate (vaterite) microsponges, Adv. Mater. 11 (1999) 324–328.
[18] H.J. Fan, U. Gösele, M. Zacharias, Formation of nanotubes and hollow nanoparticles based on kirkendall and diffusion processes: a review, Small 3 (2007) 1660–1671.
[19] K.-Y. Niu, J. Park, H. Zheng, A.P. Alivisatos, Revealing bismuth oxide hollow nanoparticle formation by the kirkendall effect, Nano Lett. 13 (2013) 5715–5719.
[20] C.C. Yec, H.C. Zeng, Synthesis of complex nanomaterials via Ostwald ripening, J. Mater. Chem. A 2 (2014) 4843–4851.
[21] Z. Yin, J. Zhu, Q. He, X. Cao, C. Tan, H. Chen, Q. Yan, H. Zhang, Graphene-based materials for solar cell applications, Adv. Energy Mater. 4 (2014) 1300574–1300592.
[22] Y. Sun, S. Gao, F. Lei, C. Xiao, Y. Xie, Ultrathin two-dimensional inorganic materials: new opportunities for solid state nanochemistry, Acc. Chem. Res. 48 (2015) 3–12.
[23] J. Zhu, L. Bai, Y. Sun, X. Zhang, Q. Li, B. Cao, W. Yan, Y. Xie, Topochemical transformation route to atomically thick Co_3O_4 nanosheets realizing enhanced lithium storage performance, Nanoscale 5 (2013) 5241–5246.
[24] Y. Sun, S. Gao, F. Lei, J. Liu, L. Liang, Y. Xie, Atomically-thin non-layered cobalt oxide porous sheets for highly efficient oxygen-evolving electrocatalysts, Chem. Sci. 5 (2014) 3976–3982.
[25] T. Yu, B. Lim, Y. Xia, Aqueous-phase synthesis of single-crystal ceria nanosheets, Angew. Chem. Int. Ed. 49 (2010) 4484–4487.
[26] Y. Sun, Z. Sun, S. Gao, H. Cheng, Q. Liu, J. Piao, T. Yao, C. Wu, S. Hu, S. Wei, Y. Xie, Fabrication of flexible and freestanding zinc chalcogenide single layers, Nat. Commun. 3 (2012) 1057–1063.
[27] S.-J. Kim, I.-S. Hwang, C.W. Na, I.-D. Kim, Y.C. Kang, J.-H. Lee, Ultrasensitive and selective C_2H_5OH sensors using Rh-loaded In_2O_3 hollow spheres, J. Mater. Chem. 21 (2011) 18560–18567.
[28] Z. Guo, J. Liu, Y. Jia, X. Chen, F. Meng, M. Li, J. Liu, Template synthesis, organic gas-sensing and optical properties of hollow and porous In_2O_3 nanospheres, Nanotechnology 19 (2008) 345704–345712.
[29] T. Zhang, F. Gu, F. Han, Z. Wang, G. Guo, Synthesis, characterization and alcohol-sensing properties of rare earth doped In_2O_3 hollow spheres, Sens. Actuators B: Chem. 177 (2013) 1180–1188.
[30] W.J. Tseng, T.-T. Tseng, H.-M. Wu, Y.-C. Her, T.-J. Yang, Facile synthesis of monodispersed In_2O_3 hollow spheres and application in photocatalysis and gas sensing, J. Am. Ceram. Soc. 96 (2013) 719–725.
[31] P. Zhao, T. Huang, K. Huang, Fabrication of indium sulfide hollow spheres and their conversion to indium oxide hollow spheres consisting of multipore nanoflakes, J. Phys. Chem. C 111 (2007) 12890–12897.
[32] B. Li, Y. Xie, M. Jing, G. Rong, Y. Tang, G. Zhang, In_2O_3 hollow microspheres: synthesis from designed In(OH)$_3$ precursors and applications in gas sensors and photocatalysis, Langmuir 22 (2006) 9380–9385.
[33] A. Gurlo, G. Miehe, R. Riedel, Surfactant-free self-assembly route to hollow In_2O_3 microspheres, Chem. Commun. (2009) 2747–2749.
[34] Y. Cao, J. Zhao, X. Zou, P.-P. Jin, H. Chen, R. Gao, L.-J. Zhou, Y.-C. Zou, G.-D. Li, Synthesis of porous In_2O_3 microspheres as a sensitive material for early warning of hydrocarbon explosions, RSC Adv. 5 (2015) 5424–5431.
[35] X.-X. Zou, G.-D. Li, Y.-N. Wang, J. Zhao, C. Yan, M.-Y. Guo, L. Li, J.-S. Chen, Direct conversion of urea into graphitic carbon nitride over mesoporous TiO_2 spheres under mild condition, Chem. Commun. 47 (2011) 1066–1068.
[36] X.-X. Zou, G.-D. Li, K.-X. Wang, L. Li, J. Su, J.-S. Chen, Light-induced formation of porous TiO_2 with superior electron-storing capacity, Chem. Commun. 46 (2010) 2112–2114.
[37] J. Su, X.-X. Zou, G.-D. Li, L. Li, J. Zhao, J.-S. Chen, Porous vanadium-doped titania with active hydrogen: a renewable reductant for chemoselective hydrogenation of nitroarenes under ambient conditions, Chem. Commun. 48 (2012) 9032–9034.
[38] J. Su, X. Zou, G.-D. Li, Y.-M. Jiang, Y. Cao, J. Zhao, J.-S. Chen, Room-temperature spontaneous crystallization of porous amorphous titania into a high-surface-area anatase photocatalyst, Chem. Commun. 49 (2013) 8217–8219.

[39] X.-X. Zou, G.-D. Li, J. Zhao, P.-P. Wang, Y.-N. Wang, L.-J. Zhou, J. Su, L. Li, J.-S. Chen, Light-driven transformation of ZnS-cyclohexylamine nanocomposite into zinc hydroxysulfate: a photochemical route to inorganic nanosheets, Inorg. Chem. 50 (2011) 9106–9113.

[40] M. Klaumünzer, M. Mačkovicí, P. Ferstl, M. Voigt, E. Spiecker, B. Meyer, W. Peukert, Phase transition behavior and oriented aggregation during precipitation of In(OH)₃ and InOOH nanocrystals, J. Phys. Chem. C 116 (2012) 24529–24537.

[41] P. Song, Q. Wang, Z. Yang, Biomorphic synthesis and gas response of In₂O₃ microtubules using cotton fibers as templates, Sens. Actuators B: Chem. 168 (2012) 421–428.

[42] A. Shanmugasundaram, P. Basak, S.V. Manorama, B. Krishna, S. Sanyadanam, Hierarchical mesoporous In₂O₃ with enhanced CO sensing and photocatalytic performance: distinct morphologies of In(OH)₃ via self assembly coupled in situ solid–solid transformation, ACS Appl. Mater. Interfaces 7 (2015) 7679–7689.

[43] X. Xu, P. Zhao, D. Wang, P. Sun, L. You, Y. Sun, X. Liang, F. Liu, H. Chen, G. Lu, Preparation and gas sensing properties of hierarchical flower-like In₂O₃ microspheres, Sens. Actuators B: Chem. 176 (2013) 405–412.

[44] S. Park, S. Kim, G.-J. Sun, C. Lee, Synthesis, structure, and ethanol gas sensing properties of In₂O₃ nanorods decorated with Bi₂O₃ nanoparticles, ACS Appl. Mater. Interfaces 7 (2015) 8138–8146.

[45] Y. Li, J. Xu, J. Chao, D. Chen, S. Ouyang, J. Ye, G. Shen, High-aspect-ratio single-crystalline porous In₂O₃ nanobelts with enhanced gas sensing properties, J. Mater. Chem. 21 (2011) 12852–12857.

[46] S.-J. Kim, I.-S. Hwang, J.-K. Choi, Y.C. Kang, J.-H. Lee, Enhanced C₂H₅OH sensing characteristics of nano-porous In₂O₃ hollow spheres prepared by sucrose-mediated hydrothermal reaction, Sens. Actuators B: Chem. 155 (2011) 512–518.

[47] J. Liu, Z. Guo, K. Zhu, W. Wang, C. Zhang, X. Chen, Highly porous metal oxide polycrystalline nanowire films with superior performance in gas sensors, J. Mater. Chem. 21 (2011) 11412–11417.

[48] A. Shanmugasundaram, B. Ramireddy, P. Basak, S.V. Manorama, S. Srinath, Hierarchical In(OH)₃ as a precursor to mesoporous In₂O₃ nanocubes: a facile synthesis route, mechanism of self-assembly, and enhanced sensing response toward hydrogen, J. Phys. Chem. C 118 (2014) 6909–6921.

[49] J. Zai, J. Zhu, R. Qi, X. Qian, Nearly monodispersed In(OH)₃ hierarchical nanospheres and nanocubes: tunable ligand-assisted synthesis and their conversion into hierarchical In₂O₃ for gas sensing, J. Mater. Chem. A 1 (2013) 735–745.

[50] W. Yang, P. Wan, X. Zhou, J. Hu, Y. Guan, L. Feng, Self-assembled In₂O₃ truncated octahedron string and its sensing properties for formaldehyde, Sens. Actuators B: Chem. 201 (2014) 228–233.

[51] S. Wang, B. Xiao, T. Yang, P. Wang, C. Xiao, Z. Li, R. Zhao, M. Zhang, Enhanced HCHO gas sensing properties by Ag-loaded sunflower-like In₂O₃ hierarchical nanostructures, J. Mater. Chem. A 2 (2014) 6598–6604.

[52] J. Cao, H. Dou, H. Zhang, H. Mei, S. Liu, T. Fei, R. Wang, L. Wang, T. Zhang, Controllable synthesis and HCHO-sensing properties of In₂O₃ micro/nanotubes with different diameters, Sens. Actuators B: Chem. 198 (2014) 180–187.

[53] M. Pashchanka, R.C. Hoffmann, A. Gurlo, J.J. Schneider, Molecular based, chimie douce approach to 0D and 1D indium oxide nanostructures. Evaluation of their sensing properties towards CO and H₂, J. Mater. Chem. 20 (2010) 8311–8319.

[54] K.-I. Choi, H.-R. Kim, J.-H. Lee, Enhanced CO sensing characteristics of hierarchical and hollow In₂O₃ microspheres, Sens. Actuators B: Chem. 138 (2009) 497–503.

[55] H.-Y. Lai, C.-H. Chen, Highly sensitive room-temperature CO gas sensors: Pt and Pd nanoparticle-decorated In₂O₃ flower-like nanobundles, J. Mater. Chem. 22 (2012) 13204–13208.

[56] F. Fang, L. Bai, H. Sun, Y. Kuang, X. Sun, T. Shi, D. Song, P. Guo, H. Yang, Z. Zhang, Y. Wang, J. Luo, J. Zhu, Hierarchically porous indium oxide nanolamellas with ten-parts-per-billion-level formaldehyde-sensing performance, Sens. Actuators B: Chem. 206 (2015) 714–720.

Biographies

Xue Wang is a master student in State Key Laboratory of Inorganic Synthesis & Preparative Chemistry, Jilin University in China. She has majored in the synthesis of hollow nanomaterials.

Yuying Meng is currently a Ph.D. candidate in school of materials science, South China University of Technology in China. She has been a visiting student in Rutgers, The State University of New Jersey for two years, from 11/2012 to 11/2014. Her research interests focus on the design and synthesis of carbon-based nanomaterials for renewable energy applications, as well as magnetic nanomaterials.

Guo-Dong Li is a full professor at State Key Lab of Inorganic Synthesis & Preparative Chemistry, College of Chemistry, Jilin University in China. He received his B.Sc. (1995), M.Sc. (1998) and Ph.D. (2001) from Jilin University. His research interests include chemical sensors, lithium batteries, photocatalysts.

Yongcun Zou is a Postdoctoral Scholar in college of electronic science & engineering, Jilin University in China. He received his Ph.D. from Jilin University (China) in 06/2014.

Yang Cao is a currently a Ph.D. candidate in State Key Laboratory of Inorganic Synthesis & Preparative Chemistry, Jilin University in China. His research interest is the synthesis of sensing nanomaterials.

Xiaoxin Zou was awarded a Ph.D. in Inorganic Chemistry from Jilin University (China) in 06/2011; and then moved to the University of California, Riverside and Rutgers, The State University of New Jersey as a Postdoctoral Scholar from 07/2011 to 10/2013. He is currently an associate professor in Jilin University. His research interests focus on the design and synthesis of noble metal-free, nanostructured and/or nanoporous materials for water splitting and renewable energy applications.